The Astrophysical Journal Letters, 997:L47 (14pp), 2026 February 1 https://doi.org/10.3847/2041-8213/ae313a

exoALMA. XIX. Confirmation of Non-thermal Line Broadening in the DM Tau Protoplanetary Disk

Caitlyn Hardiman[1], Christophe Pinte[2], Daniel J. Price[1], Thomas Hilder[1], Iain Hammond[1,3], Taïssa Danilovich[1,4], Sean M. Andrews[5], Richard Teague[6], Giovanni Rosotti[7], Mario Flock[3], Gianni Cataldi[8], Jaehan Bae[9], Marcelo Barraza-Alfaro[6], Myriam Benisty[3,10], Nicolás Cuello[2], Pietro Curone[11], Ian Czekala[12], Stefano Facchini[13], Daniele Fasano[3,10], Misato Fukagawa[8], Maria Galloway-Sprietsma[9], Himanshi Garg[1], Cassandra Hall[14,15,16], Jane Huang[17], John D. Ilee[18], Andres F. Izquierdo[9,19,20,28], Kazuhiro Kanagawa[21], Geoffroy Lesur[2], Giuseppe Lodato[7], Cristiano Longarini[7,22], Ryan Loomis[23], Francois Menard[2], Ryuta Orihara[21], Jochen Stadler[10,20], Hsi-Wei Yen[24], Gaylor Wafflard- Fernandez[2], David J. Wilner[5], Andrew J. Winter[25], Lisa Wölfer[6], Tomohiro C. Yoshida[8], and Brianna Zawadzki[26,27]

[1] School of Physics & Astronomy, Monash University, Clayton VIC 3800, Australia; caitlyn.hardiman@monash.edu
[2] Univ. Grenoble Alpes, CNRS, IPAG, 38000 Grenoble, France
[3] Max-Planck Institute for Astronomy (MPIA), Königstuhl 17, 69117 Heidelberg, Germany
[4] Institute of Astronomy, KU Leuven, Celestijnenlaan 200D, 3001 Leuven, Belgium
[5] Center for Astrophysics—Harvard & Smithsonian, Cambridge, MA 02138, USA
[6] Department of Earth, Atmospheric, and Planetary Sciences, Massachusetts Institute of Technology, Cambridge, MA 02139, USA
[7] Dipartimento di Fisica, Università degli Studi di Milano, Via Celoria 16, 20133 Milano, Italy
[8] National Astronomical Observatory of Japan, 2-21-1 Osawa, Mitaka, Tokyo 181-8588, Japan
[9] Department of Astronomy, University of Florida, Gainesville, FL 32611, USA
[10] Université Côte d'Azur, Observatoire de la Côte d'Azur, CNRS, Laboratoire Lagrange, France
[11] Departamento de Astronomía, Universidad de Chile, Camino El Observatorio 1515, Las Condes, Santiago, Chile
[12] School of Physics & Astronomy, University of St. Andrews, North Haugh, St. Andrews KY16 9SS, UK
[13] Dipartimento di Fisica, Universitá degli Studi di Milano, Via Celoria 16, I-20133 Milano, Italy
[14] Department of Physics and Astronomy, The University of Georgia, Athens, GA 30602, USA
[15] Center for Simulational Physics, The University of Georgia, Athens, GA 30602, USA
[16] Institute for Artificial Intelligence, The University of Georgia, Athens, GA, 30602, USA
[17] Department of Astronomy, Columbia University, 538 W. 120th Street, Pupin Hall, New York, NY 10027, USA
[18] School of Physics and Astronomy, University of Leeds, Leeds, LS2 9JT, UK
[19] Leiden Observatory, Leiden University, P.O. Box 9513, NL-2300 RA Leiden, The Netherlands
[20] European Southern Observatory, Karl-Schwarzschild-Str. 2, D-85748 Garching bei München, Germany
[21] College of Science, Ibaraki University, 2-1-1 Bunkyo, Mito, Ibaraki 310-8512, Japan
[22] Institute of Astronomy, University of Cambridge, Madingley Rd, CB30HA, Cambridge, UK
[23] National Radio Astronomy Observatory, Charlottesville, VA 22903, USA
[24] Academia Sinica Institute of Astronomy & Astrophysics, 11F of Astronomy-Mathematics Building, AS/NTU, No. 1, Sec. 4, Roosevelt Road, Taipei 10617, Taiwan
[25] Astronomy Unit, School of Physics and Astronomy, Queen Mary University of London, London E1 4NS, UK
[26] Department of Astronomy, Van Vleck Observatory, Wesleyan University, 96 Foss Hill Drive, Middletown, CT 06459, USA
[27] Department of Astronomy & Astrophysics, 525 Davey Laboratory, The Pennsylvania State University, University Park, PA 16802, USA
Received 2025 November 5; revised 2025 December 18; accepted 2025 December 18; published 2026 January 30

Abstract

Turbulence is expected to transport angular momentum and drive mass accretion in protoplanetary disks. One way to directly measure turbulent motion in disks is through molecular line broadening. DM Tau is one of only a few disks with claimed detection of nonthermal line broadening of $0.25c_s$–$0.33c_s$, where c_s is the sound speed. Using the radiative transfer code MCFOST within a Bayesian inference framework that evaluates over five million disk models to efficiently sample the parameter space, we fit high-resolution (0.″15, 28 m s^{-1}) ^{12}CO $J = 3$–2 observations of DM Tau from the exoALMA Large Program. This approach enables us to simultaneously constrain the disk structure and kinematics, revealing a significant nonthermal contribution to the line width of $\sim 0.4c_s$, inconsistent with purely thermal motions. Using the CO-based disk structure as a starting point, we reproduce the CS $J = 7$–6 emission well, demonstrating that the CS (which is more sensitive to nonthermal motions than CO) agrees with the turbulence inferred from the CO fit. Establishing a well-constrained background disk model further allows us to identify residual structures in the moment maps that deviate from the expected emission, revealing localized perturbations that may trace forming planets. This framework provides a powerful general approach for extracting disk structure and nonthermal broadening directly from molecular line data and can be applied to other disks with high-quality observations.

Unified Astronomy Thesaurus concepts: Protoplanetary disks (1300); High angular resolution (2167); CO line emission (262); T Tauri stars (1681)

1. Introduction

Turbulent motions are one of the main contenders for driving angular momentum transport in protoplanetary disks, with α-disk models (N. I. Shakura & R. A. Sunyaev 1973;

[28] NASA Hubble Fellowship Program Sagan Fellow.

J. E. Pringle 1981) parameterizing the bulk disk viscosity ν in terms of the dimensionless parameter α via

$$\nu = \alpha c_s H, \quad (1)$$

where c_s is the sound speed and H is the pressure scale height. This relation assumes that the largest-scale motions would be less than or equal to the scale height of the disk, H, and typical motions would be subsonic, implying $\alpha \in [0, 1]$. The actual value of α and the source of the turbulence itself are poorly constrained.

High spectral and spatial resolution surveys such as exoALMA (R. Teague et al. 2025) now enable direct comparisons between observations and theoretical models of turbulence in protoplanetary disks (M. Barraza-Alfaro et al. 2025). One of the most prominent proposed mechanisms is the magnetorotational instability (MRI; S. A. Balbus & J. F. Hawley 1991, 1998). Other candidates include gravitational instability (see K. Kratter & G. Lodato 2016, for a review), embedded planets (J. Goodman & R. R. Rafikov 2001), the vertical shear instability (VSI; R. P. Nelson et al. 2013; M. H. R. Stoll & W. Kley 2014; M. Flock et al. 2017), the convective overstability, and the subcritical baroclinic instability (T. Pfeil & H. Klahr 2019). Determining which of these mechanisms actually operate in disks requires observational constraints on the strength and spatial distribution of turbulence.

We can *indirectly* measure α for protoplanetary disks via observations of accretion rates onto their host stars, which C. F. Manara et al. (2016) have found to span a range of 10^{-11} to $10^{-7}\,M_\odot\,\mathrm{yr}^{-1}$. This can then be related to an α as $\dot{M}_{\rm acc} = 3\pi\nu\Sigma$, either assuming or fitting simultaneously for a surface density profile Σ (e.g., N. van der Marel et al. 2021). Similarly, one can match the observed disk lifetime to that predicted from self-similar disk evolution given values of $M_{\rm disk}$ and $\dot{M}_{\rm acc}$ (L. Hartmann et al. 1998; C. F. Manara et al. 2023). Based on these approaches, estimates of α typically fall in the range 10^{-4} to 10^{-3} (see review by G. P. Rosotti 2023). However, it is important to note that these measurements are instantaneous values that may vary significantly with time, particularly if the disk undergoes episodic accretion events such as FU Ori–type outbursts.

Another indirect method of constraining turbulence in disks is by observing the height of the dust layer in edge-on disks, as turbulence will stir the dust up from the disk midplane (e.g., C. Pinte et al. 2016; M. Villenave et al. 2025). Dust settling prescriptions (B. Dubrulle et al. 1995; S. Fromang & R. P. Nelson 2009) relate the scale height of the dust to the gas scale height via a combination of an α and the stopping time of the dust grains where $H \propto \sqrt{\alpha/\tau_s}$. Infrared and millimeter imaging of edge-on disks clearly shows that grains larger than $\approx$100 μm are settled in the midplane of the disk (M. Villenave et al. 2020, 2022, 2024; G. Duchêne et al. 2024), with the dust scale height up to an order of magnitude smaller than that of the gas, again indicating weak stirring of the dust layer, implying $\alpha \lesssim 10^{-4}$.

The first attempt to directly measure nonthermal molecular line broadening in protoplanetary disks was made by A. M. Hughes et al. (2011) using pre–Atacama Large Millimeter/submillimeter Array (ALMA) Submillimeter Array observations of the TW Hya and HD 163296 disks, which found an upper limit of $\lesssim 0.1c_s$ and a tentative detection of $\sim 0.4c_s$, respectively. With the advent of ALMA, higher spatial and spectral resolution data enabled much tighter constraints: K. M. Flaherty et al. (2015, 2017) reported $v_{\rm turb} \lesssim 0.03c_s$–$0.06c_s$ in HD 163296; and R. Teague et al. (2016) reported $v_{\rm turb}$ between $0.2c_s$ and $0.4c_s$ in TW Hya, revised downward to $\lesssim 0.08c_s$ ($\alpha \lesssim 0.007$) by K. M. Flaherty et al. (2018). Most recently, K. Flaherty et al. (2024) and T. Paneque-Carreño et al. (2024) reported $0.18c_s$–$0.3c_s$ and $0.4c_s$–$0.6c_s$, respectively, around IM Lup.

As one of the few disks with a measured nonzero turbulence, DM Tau offers the opportunity to probe nonthermal line broadening using the high-resolution data from exoALMA. DM Tau is a low-mass ($\approx 0.5\,M_\odot$) T Tauri star with a large ($\approx$300 au) protoplanetary disk featuring an inner disk and three pairs of gaps and rings seen in continuum emission (S. M. Andrews et al. 2011; T. Kudo et al. 2018; L. Francis et al. 2022; P. Curone et al. 2025). Its accretion rate has been measured as $\dot{M}_{\rm acc} = 10^{-8.2}\,M_\odot\,\mathrm{yr}^{-1}$ (C. F. Manara et al. 2014). Line-broadening measurements by K. Flaherty et al. (2020) found $0.25c_s$–$0.33c_s$ (equivalent to 0.06–0.11 in α), using a fixed stellar mass of 0.54 $M_\odot$. S. Guilloteau et al. (2012) obtained consistent results using CS, a heavier molecule less sensitive to thermal broadening than CO, finding a turbulent line width of $\sim 0.14\,\mathrm{km\,s}^{-1}$ at 300 au. However, this is discrepant with the inferred value of α needed to explain the continuum gap depth at 21 au if carved by a planet ($\alpha \lesssim 10^{-3}$; L. Francis et al. 2022); we note, however, that the former measurements probe the outer disk while the latter constraint applies to the inner regions, and these estimates are therefore unlikely to correspond to the same radial location.

When modeling spatially resolved disks, accurately constraining nonthermal line broadening requires distinguishing its contribution from other factors that influence the observed kinematics, such as the stellar mass and disk temperature structure. The high angular and spectral resolution of the exoALMA Large Program (R. Teague et al. 2025) provides the level of detail needed to disentangle these effects. We use these data to quantify the level of nonthermal broadening in DM Tau and to test whether a disk structure inferred from CO can also reproduce the emission from heavier molecules such as CS.

The Letter is organized as follows: Section 2 describes the data, the modeling approach, and the image-plane fitting methodology. Section 3 presents the inferred nonthermal line broadening from CO and the CS modeling results. In Section 4, we interpret these results in the context of disk kinematics and potential planet–disk interactions, and we summarize our findings in Section 5.

2. Methods

2.1. Observations

We used ^{12}CO $J = 3$–2 and CS $J = 7$–6 observations of DM Tau from the exoALMA Large Program, with the data reduction detailed in R. A. Loomis et al. (2025). For CO, we selected a primary-beam-corrected cube with a spatial resolution of 0.″15 and a spectral resolution of $28\,\mathrm{m\,s}^{-1}$. To reduce computational cost, we fit only 17 evenly spaced representative velocity channels spanning 3.5–8.5 $\mathrm{km\,s}^{-1}$ around the systemic velocity ($v_{\rm syst} = 6.03\,\mathrm{km\,s}^{-1}$; A. F. Izquierdo et al. 2025), which capture the bulk of the emission. We restricted ourselves to a 15.″0 box centered on the disk to encompass the full CO-emitting region. The CS cube used was also primary beam corrected, at the same spatial resolution but with a spectral resolution of

100 m s^{-1}, needed to obtain sufficient signal-to-noise ratio for this comparatively faint line. A 6.″0 box was used to capture the full CS emission while limiting data volume.

2.2. Radiative Transfer Modeling

We used the radiative transfer code MCFOST (C. Pinte et al. 2006, 2009) to generate disk models of the ^{12}CO and CS exoALMA data for DM Tau, assuming an unperturbed smooth disk containing no planets or gaps. Both the models and the data include continuum emission, which we did not subtract (as in previous works; see S. Guilloteau et al. 2012; K. Flaherty et al. 2020), since the continuum is much more compact than the ^{12}CO gas (119 au vs. 580 au enclosing 68% of the flux; P. Curone et al. 2025; C. Longarini et al. 2025) and only affects the innermost regions of the disk.

We used a tapered-edge disk model with the disk surface density profile Σ set according to the self-similar solution of D. Lynden-Bell & J. E. Pringle (1974; see, e.g., L. Hartmann et al. 1998; C. F. Manara et al. 2023) given by

$$\Sigma(r) = \frac{M_0(2-\gamma)}{2\pi R_c^2}\left(\frac{r}{R_c}\right)^{-\gamma} \exp\left[-\left(\frac{r}{R_c}\right)^{2-\gamma}\right], \quad (2)$$

which exponentially decreases for radii r greater than the critical radius R_c. Parameter γ is the power-law index of the surface density and of the outer taper, and M_0 is the disk mass. We let our disk extend from an inner radius $R_{\rm in}$ of 5 au to $R_{\rm out}$ of 1000 au, noting that the outer edge is more properly constrained by R_c, or the surface density gradient itself as γ approaches 2. We also assumed a Gaussian vertical density profile parameterized by a scale height with a radial dependence given by $h(r) = h_0(r/r_0)^{\Psi}$ at a reference radius of $r_0 = 150$ au, where Ψ is the flaring exponent.

The disk temperature structure was computed by MCFOST assuming local thermodynamic equilibrium (LTE). This temperature distribution, combined with the density structure, determines the regions affected by molecular processes. We included molecular photodissociation and photodesorption and imposed CO freezeout in regions where the temperature drops below 20 K, using a depletion factor $f_{\rm remain}$ that sets the fraction of gas remaining in the gas phase (following C. Pinte et al. 2018). By default, $f_{\rm remain} = 0$, meaning that all CO in these regions is frozen out. For CS, we adopted a freezeout temperature of 30 K, near the lower end of the range of values reported in the literature (20–30 K from excitation/evaporation estimates, S. Guilloteau et al. 2012; R. Le Gal et al. 2019; 50–60 K from other observational studies, R. T. Garrod & E. Herbst 2006; G. van der Plas et al. 2014).

The external UV field was modeled as the B. T. Draine (1978) interstellar radiation field scaled by a factor $\chi_{\rm ISM}$, which contributes extra heating in the disk's upper layers.

Vertical dust settling was implemented using the prescription given in Equation (19) of S. Fromang & R. P. Nelson (2009), where the amount of dust settling is controlled by $\alpha_{\rm dust}$, and the Schmidt number in their Equation (20) was set to a fixed value of $Sc = 1.5$. In MCFOST, $\alpha_{\rm dust}$ only controls the diffusion coefficient for the dust and does not contribute to additional line broadening, which is implemented as an independent parameter (described in Section 2.3).

We employed a dust population in our models from the DiscAnalysis (DIANA) project (P. Woitke et al. 2016) for DM Tau, which consisted of 79% silicates (J. Dorschner et al. 1995) and 21% amorphous carbon (V. G. Zubko et al. 1996), with 25% grain porosity. Following their setup, dust properties were calculated using the distribution of hollow spheres formalism (M. Min et al. 2005) with a maximum void fraction of 0.8, and the grain size distribution was set as $dN(a) \propto a^{-3.7}\, da$ for grain sizes a between $a_{\rm min} = 0.0152\ \mu$m and $a_{\rm max} = 3990\ \mu$m. We also used the DIANA stellar spectrum file and corresponding effective stellar temperature of 3779 K.[29]

In addition to the parameters already described, we allowed the disk orientation (inclination i and position angle PA), stellar properties (stellar mass $M_\star$ and radius $R_\star$, the latter of which allows the stellar luminosity to vary), and gas properties (gas mass $M_{\rm gas}$, gas-to-dust mass ratio, and CO abundance $X_{\rm CO}$) to vary when fitting the CO emission. Once the CO model was determined, we used it as the baseline for modeling CS, keeping the temperature and density distributions fixed and only fitting for the molecular abundance $X_{\rm CS}$ and the fraction of gas-phase CS in the freezeout region $f_{\rm remain}$. We assumed constant abundances for both CO and CS throughout the disk, i.e., the molecular number density at each location is given by the product of the gas density and a fixed abundance, modulated by freezeout, photodissociation, and photodesorption where relevant.

Table 1 lists all of the parameters we allowed to vary for both the CO and CS fits, including the line-broadening parameter $f_{\rm turb}$ we will describe more fully in Section 2.3. We aimed to allow as much freedom in the model parameters as possible to avoid any degeneracies going unnoticed. Importantly, we included stellar mass as a variable parameter rather than using a literature value, which was the approach of K. Flaherty et al. (2020) and L. Francis et al. (2022). In addition to using the discussed values from the DIANA project, we used a fixed distance to DM Tau of 144.0 pc from Gaia DR3 (Gaia Collaboration et al. 2023) and a systemic velocity of 6.03 km s^{-1} (A. F. Izquierdo et al. 2025).

2.3. Line-broadening Parameter

Among the free parameters listed in Table 1 is the nonthermal line-broadening factor, $f_{\rm turb}$, which parameterizes the level of turbulent motion in the disk. We assume a Gaussian line profile of width

$$\Delta V = \sqrt{\frac{2k_{\rm B}T(r,z)}{m_{\rm CO}} + v_{\rm turb}^2}, \quad (3)$$

where $k_{\rm B}$ is the Boltzmann constant, T is the local kinetic temperature, $m_{\rm CO}$ is the mass of the CO molecule, and $v_{\rm turb}$ is the nonthermal line broadening. ΔV is $\sqrt{2}\,\sigma$, where σ is the Gaussian standard deviation. Our prescription for $v_{\rm turb}$ follows theoretical predictions (J. B. Simon et al. 2015; M. Flock et al. 2017) where the turbulence scales with the sound speed

$$v_{\rm turb} = f_{\rm turb} \times \sqrt{\frac{k_{\rm B}T(r,z)}{\mu m_h}}, \quad (4)$$

where $f_{\rm turb}$ is a constant and $\mu = 2.3$ is the mean molecular weight in units of the proton mass m_h.

[29] The stellar spectrum file and the MCFOST parameter file used for the DIANA model are found at the Monash University Bridges repository: doi:10.26180/30908507.

Table 1
Model Parameters, Priors, Bounds, and Posterior Results for Our Fits of the DM Tau Disk

Parameter	Prior	Bounds	Posterior Median
CO Emission Fit			
i (deg)	$\mathcal{N}(39, 3)$	(0, 180)	$39.7^{+0.7}_{-0.7}$
$M_\star$ ($M_\odot$)	$\mathcal{N}(0.45, 0.05)$	(0, ∞)	$0.483^{+0.01}_{-0.01}$
h_0 (au)	$\mathcal{N}(10, 2.5)$	(0, ∞)	$20.6^{+0.6}_{-0.9}$
R_c (au)	$\mathcal{N}(240, 20)$	(7, ∞)	$336.4^{+27.0}_{-44.9}$
Ψ	$\mathcal{N}(1.315, 0.05)$	(1, 2)	$1.16^{+0.023}_{-0.036}$
PA (deg)	$\mathcal{N}(155.7, 3)$	(0, 360)	$155.4^{+0.2}_{-0.2}$
$\log_{10}(\alpha_{\rm dust})$	$\mathcal{N}(-4, 0.5)$	(−6, 0)	$-0.87^{+0.35}_{-0.20}$
$f_{\rm turb}$	$\mathcal{U}(0, 1)$	(0.0, 1.0)	$0.404^{+0.016}_{-0.032}$
$M_{\rm gas}$ ($M_\odot$)	$\mathcal{N}(4 \times 10^{-2}, 1 \times 10^{-2})$	(0, ∞)	$6.6^{+0.1}_{-0.1} \times 10^{-2}$
$\log_{10}(M_{\rm gas}/M_{\rm dust})$	$\mathcal{N}(2.0, 0.1)$	(0, 3)	$2.50^{+0.19}_{-0.17}$
$\log_{10}(X_{\rm CO})$	$\mathcal{N}(-4.7, 1.5)$	(−7, −2)	$-4.52^{+0.14}_{-0.07}$
$f_{\rm remain}$	$\mathcal{E}(0.2)$	(0, 1)	$0.002^{+0.001}_{-0.001}$
γ	$\mathcal{N}(1.0, 0.1)$	(0, 2)	$1.55^{+0.20}_{-0.17}$
$R_\star$ ($R_\odot$)	$\mathcal{N}(1.22, 0.1)$	(1, ∞)	$1.25^{+0.15}_{-0.13}$
$\chi_{\rm ISM}$	$\mathcal{E}(0.2)$	⋯	$0.65^{+0.08}_{-0.10}$
$\ln q$	$\mathcal{N}(-1, 0.05)$	(−3, 1)	$-1.72^{+0.08}_{-0.04}$
CS Emission Fit (Other Disk Parameters Fixed)			
$\log_{10}(X_{\rm CS})$	$\mathcal{N}(-8, 1.5)$	(−12, −2)	$-9.4126^{+0.007}_{-0.006}$
$f_{\rm remain}$	$\mathcal{E}(0.2)$	(0, 1)	$0.997^{+0.003}_{-0.012}$
$\ln q$	$\mathcal{N}(-1, 0.05)$	(−3, 1)	$-1.22^{+0.01}_{-0.01}$

Notes. CO emission and CS emission parameters are shown in separate blocks. For the CS fit, all other disk parameters were fixed to the CO best-fit values. Posterior values are the medians with 2σ uncertainties.
$\mathcal{N}(\mu, \sigma)$: normal prior with mean μ and standard deviation σ (truncated to bounds).
$\mathcal{U}(a, b)$: uniform prior between a and b.
$\mathcal{E}(\lambda)$: exponential prior with scale λ (truncated to bounds).

2.4. Parameter Estimation

The problem with trying to measure nonthermal line broadening in a disk is that $v_{\rm turb}$ may be biased by other parameters in the fit, especially the thermal structure. To account for this, we sampled the posterior distribution of the model parameters using a Markov Chain Monte Carlo (MCMC) framework, employing the affine-invariant ensemble sampler from the EMCEE[30] package (D. Foreman-Mackey et al. 2013). At each MCMC iteration, a synthetic data cube was produced with MCFOST, convolved with the observational beam, and compared to the 17 equivalent velocity channels from the observed data cube selected to span the full disk emission (see Section 2.1).

To account for the possibility that the observational noise is underestimated, we included an additional free parameter, $\ln q$, which inflates the variance in each channel. In reality, uncertainties are underestimated because we neglect the stationary covariance between neighboring pixels (e.g., T. Hilder et al. 2025); including this parameter is intended to partially compensate for this effect. With this term, the total variance is given by

$$\mathbf{s_n}^2 = \sigma_n^2 + q^2 \mathcal{M}^2, \tag{5}$$

where $\mathcal{M}$ denotes the model flux at each pixel in the convolved channel and σ_n is the measured rms of the data cube. In addition to compensating for underestimated pixel-to-pixel uncertainties, $\ln q$ partially absorbs systematic mismatches in the absolute flux scale that may arise from amplitude calibration uncertainties. Since q scales with the model flux, over- or underestimates of the total flux are partially accounted for through this term, reducing their impact on the inferred physical parameters. The parameter $\ln q$ is sampled alongside all other model parameters.

Assuming Gaussian noise, the log-likelihood is then computed as

$$\ln \mathcal{L} = -\frac{1}{2} \sum \left[\frac{(\mathcal{D} - \mathcal{M})^2}{s_n^2} + \ln(2\pi s_n^2) \right], \tag{6}$$

with $\mathcal{D}$ representing the data values in the corresponding channels.

All fits used 512 walkers. The CO and CS fits were run for a minimum of 10,000 and 6000 iterations, respectively, discarding the first 4000 as burn-in. For the main CO fit this therefore involved evaluating 5,120,000 radiative transfer models in 3D. Each model computation completed in around 4 minutes on a single CPU, in total requiring 55 days of wall time running in parallel on 256 CPUs.

3. Results

3.1. CO Fitting

We first constrain the disk structure of DM Tau by fitting the ^{12}CO $J = 3$–2 emission. Figure 1 shows representative channel maps of our best-fitting model alongside the data and residuals, with the corresponding parameters listed in Table 1. The model reproduces the overall morphology of the emission

[30] https://github.com/dfm/emcee

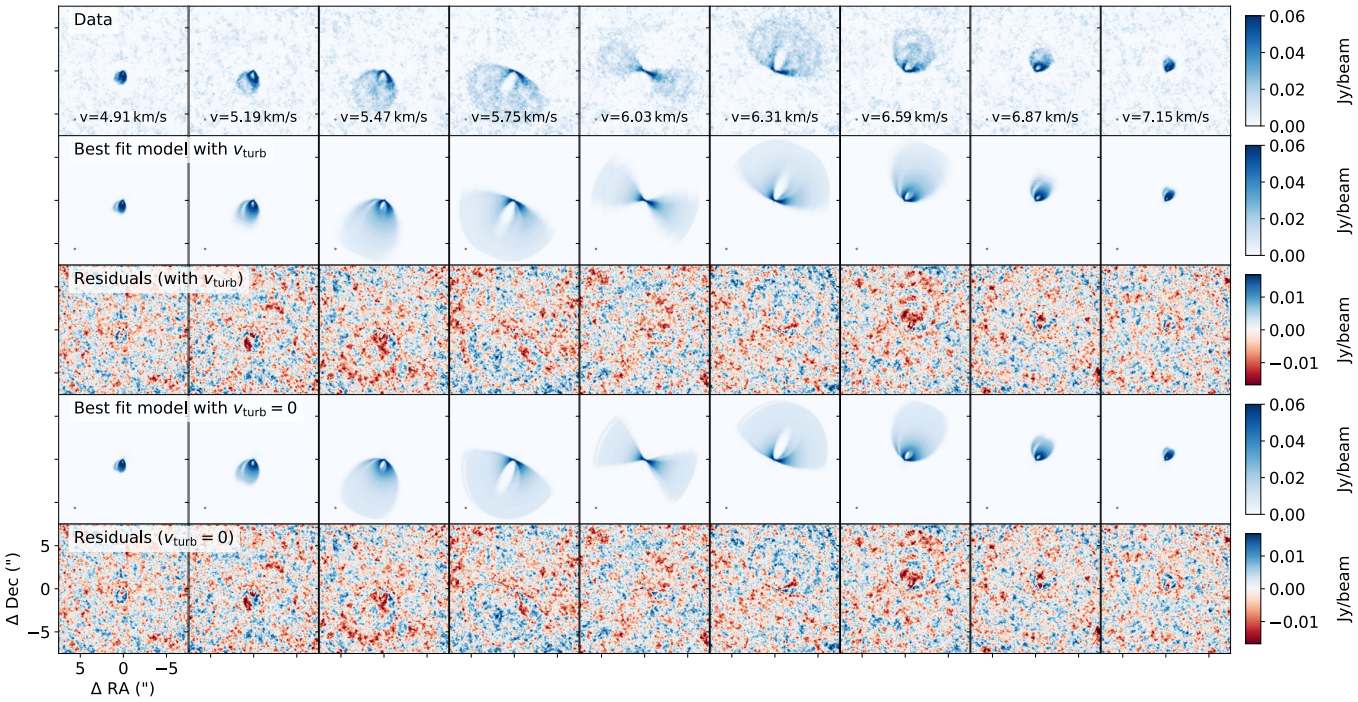

Figure 1. Channel maps of DM Tau in ^{12}CO $J = 3$–2 at 0.″15 resolution. The top row shows the observed data, the second row our best-fit model with nonzero turbulence, and the third row the residuals from subtracting this model from the data. The fourth and fifth rows show the model and residuals, respectively, for the best-fit zero-turbulence model for comparison. Each residual color bar spans $\pm 3\sigma$ flux for the data cube.

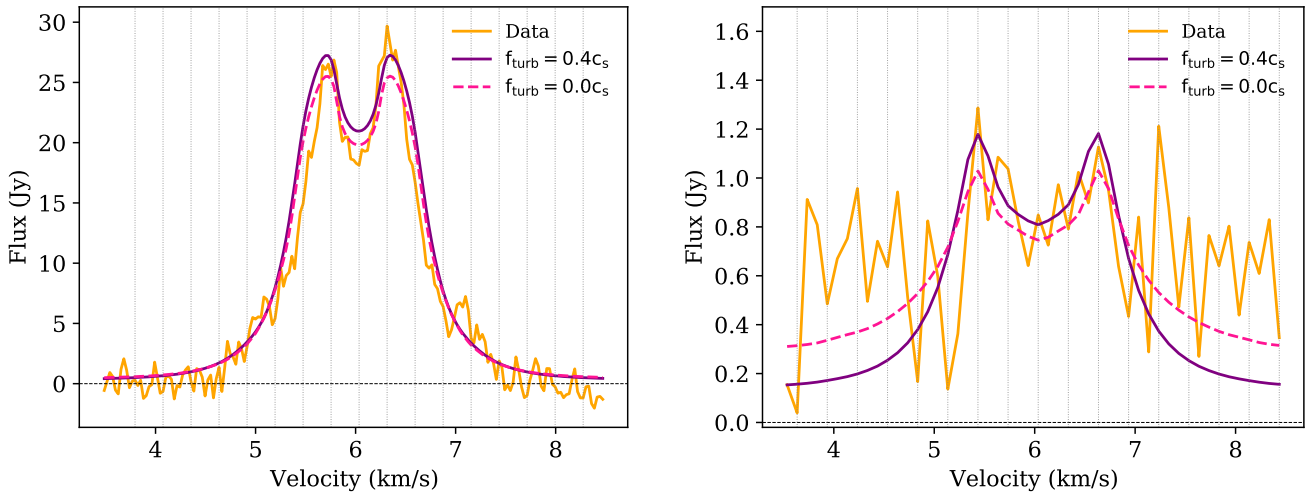

Figure 2. Comparison of observed and modeled integrated line profiles for DM Tau. Left: CO $J = 3$–2 line profile. Right: CS $J = 7$–6 line profile. The vertical dotted lines in each panel mark the velocity channels included in the fit. The agreement for CS demonstrates that the CO-derived disk structure can be directly applied to other molecular tracers, allowing differences in emission to be interpreted primarily in terms of chemistry and excitation rather than large-scale structural variations.

across all 17 channels, with the rms of the residual cube consistent with the image noise, indicating that the model captures the bulk of the emission. The integrated line profile (Figure 2, left) also shows good agreement with the data. The model slightly overestimates the total flux, with the largest discrepancy of order ∼10% in the systemic channel. This discrepancy arises from small residuals integrated over many pixels: on a per-channel basis, the standard deviation of the residuals remains consistent with the image noise (0.0056 Jy beam^{-1}), and the mean residual (0.00545 Jy beam^{-1}) is below the per-channel rms. The maximum rms in any individual channel is 0.0059 Jy beam^{-1}, which is also consistent with the image noise. The model reproduces the line wings and overall line shape well.

The posterior distribution (Appendix) shows narrow ranges for the fitted parameters, corresponding to the small uncertainties listed in Table 1. However, these represent only the statistical uncertainties within our adopted model. We neglect pixel correlations in the noise from the imaging process, which can cause underestimation by an order of magnitude (T. Hilder et al. 2025). Additionally, our smooth and axisymmetric disk model does not completely capture complex substructures in the data (J. Stadler et al. 2025). Therefore, the true uncertainties are larger than the quoted credible intervals.

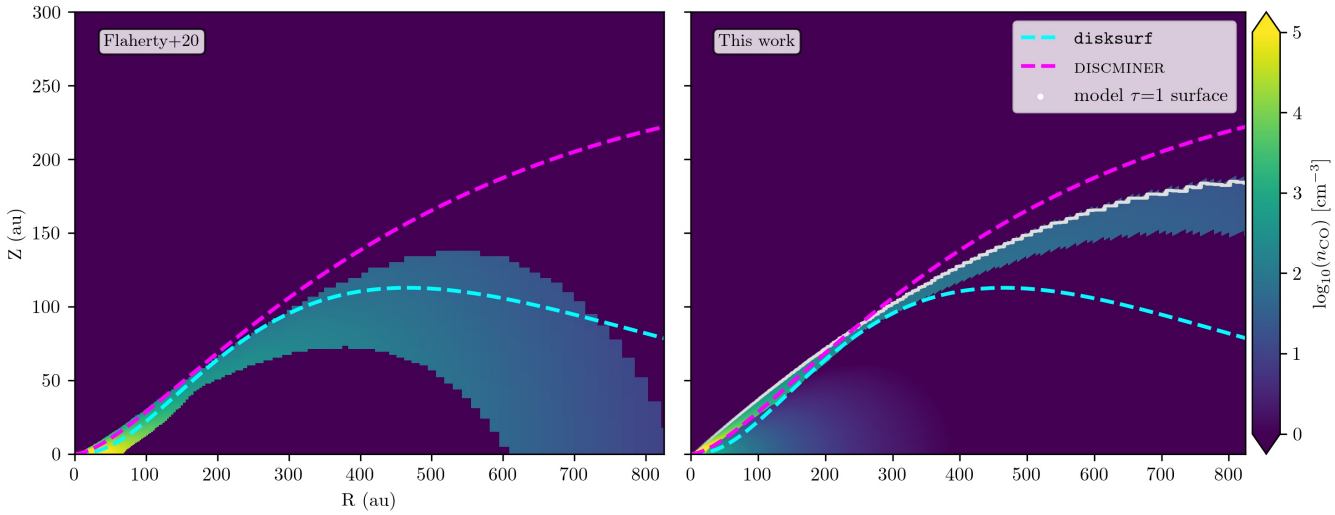

Figure 3. CO number density in DM Tau. The cyan and magenta dashed lines show the exoALMA-derived emission heights from M. Galloway-Sprietsma et al. (2025) using DISCMINER and `disksurf`. Left: $J = 2$–1 model from K. Flaherty et al. (2020). Right: Our $J = 3$–2 model.

The posterior mean inclination is $39.^{\circ}7$ and the position angle is $155.^{\circ}4$, both in excellent agreement with previous measurements (K. Flaherty et al. 2020; P. Curone et al. 2025; A. F. Izquierdo et al. 2025). The critical radius is $R_c \sim 336$ au with a surface density gradient $\gamma \sim 1.55$, indicating an extended disk with a steep outer density profile. Our best-fit stellar mass is $0.483 \pm 0.004\,M_{\odot}$, consistent with the dynamical mass obtained by C. Longarini et al. (2025) of $0.468^{+0.014}_{-0.015}$ but slightly lower than the $0.54\,M_{\odot}$ adopted by K. Flaherty et al. (2020). This difference likely reflects variations in modeling assumptions, such as the disk structure and temperature profile, rather than statistical uncertainty. Overall, this highlights that the derived parameters are sensitive to model framework and that our results cannot capture uncertainties caused by unmodeled features in the data.

Our model also constrains the global disk structure. The vertical structure is characterized by a scale height $h_0 = 20.6$ au at 150 au and a flaring index $\Psi = 1.16$, implying a moderately flared geometry.

The relatively large value of $\alpha_{\rm dust}$ results from the fact that fitting procedure for the gas disk is not sensitive to the continuum emission; hence, while the model prefers nonsettled small (micron-sized) grains, it does not imply much about the scale height of millimeter-emitting grains.

3.2. Turbulent Line Broadening and Disk Thermal Structure

A key outcome of the modeling is the constraint on the nonthermal contribution to the line width. We measure $f_{\rm turb} = 0.404^{+0.016}_{-0.032}\,c_s$, corresponding to $\alpha = 0.16^{+0.01}_{-0.02}$ and an average nonthermal broadening of $\sim$180 m s^{-1} in the CO-emitting region. To illustrate the impact of turbulence, we also ran a fit using models with no $f_{\rm turb}$ contribution. While the channel maps of the zero-turbulence model (also shown in Figure 1) are visually similar to the best-fit turbulent model, the fitting clearly favors a nonzero turbulence value. We also see this in the integrated line profile (Figure 2, left), where the model with no $f_{\rm turb}$ does not fit the peak intensity. This preference is reflected quantitatively in the Akaike information criterion (H. Akaike 1974), with the free-turbulence model strongly favored over the zero-turbulence model ($\Delta{\rm AIC} \approx 1.25 \times 10^4$), which confirms that including some level of turbulence improves the fit. Our data have a spatial resolution of $0.''15$ ($\sim$22 au at the distance of the disk), which resolves the largest disk structures but smears smaller features, and this can partially mask the subtle line broadening introduced by turbulence. Consequently, model fitting, rather than visual inspection alone, is required to robustly detect the nonthermal motions. The inferred level from our fit is even higher than the previously determined value of K. Flaherty et al. (2020), who reported $0.25c_s$–$0.33c_s$ from a parametric fit to ^{12}CO $J = 2$–1.

Figure 3 shows the CO number density of our $J = 3$–2 model (right panel) compared with the $J = 2$–1 model of K. Flaherty et al. (2020; left panel). We further overplot our model $\tau = 1$ surface (shown in white in the right panel) and the CO emission heights derived from the $J = 3$–2 exoALMA observations (M. Galloway-Sprietsma et al. 2025), obtained using DISCMINER (A. F. Izquierdo et al. 2021) and `disksurf` (R. Teague et al. 2021). Although our model and that of K. Flaherty et al. (2020) are based on different transitions, we found a negligible difference between the $\tau = 1$ surfaces of the $J = 3$–2 and $J = 2$–1 lines in our model. While the underlying CO number density in both models is of the same order of magnitude, the spatial distributions vary, due to differences in modeling assumptions and constraints and the higher spatial and spectral resolution of our exoALMA observations.

The comparison reveals an interesting trend. In the inner disk ($R \sim 250$–300 au), all four measurements—K. Flaherty et al. (2020) in $J = 2$–1, our $J = 3$–2 model, and the exoALMA emission heights—are closely aligned, suggesting that the vertical structure is able to be well constrained by a variety of modeling approaches in this region. Beyond $\sim$300 au, differences become apparent: our 3–2 model and the DISCMINER surfaces reach higher altitudes of 150–200 au, while the `disksurf` height remains lower, similar to that found by K. Flaherty et al. (2020). This suggests that differences in modeling approach and sensitivity to the diffuse outer disk gas likely drive the elevated surfaces in our model and the DISCMINER emission surface.

To examine the underlying thermal structure, Figure 4 compares the temperature distribution of our model (right)

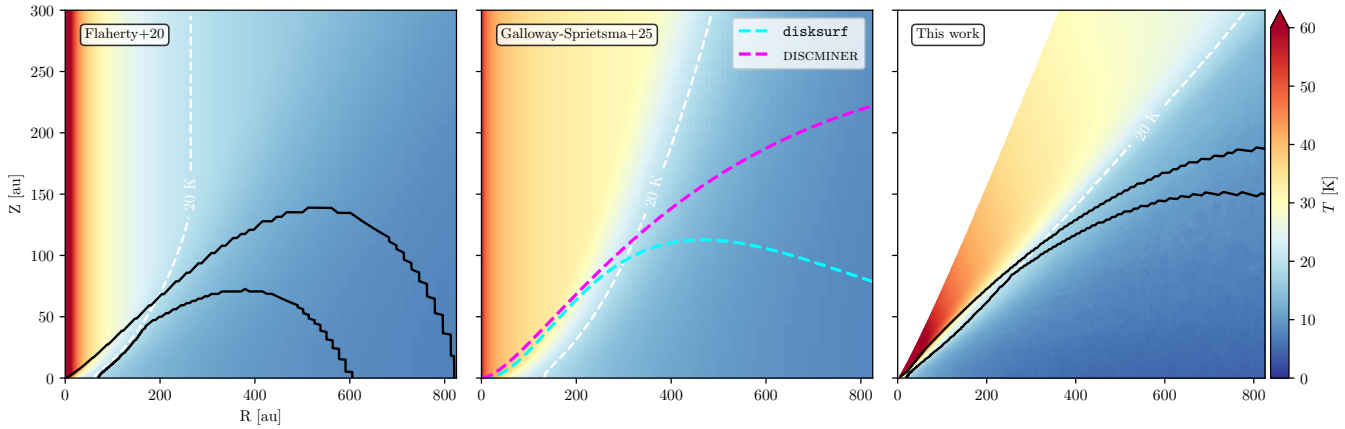

Figure 4. Comparison of temperature structures from different models. Each panel shows the gas temperature as a function of radius and height for (left to right) the models from K. Flaherty et al. (2020), M. Galloway-Sprietsma et al. (2025), and this work. The white contour indicates 20 K, which we used as our CO freezeout temperature. The black contours trace the height enclosing the top 95% of the model CO number density at each radius, highlighting the bulk CO while excluding low-density photodesorbed regions. Colored contours indicate the exoALMA emission heights.

with those from K. Flaherty et al. (2020) and the exoALMA analysis of M. Galloway-Sprietsma et al. (2025), shown in the left and middle panels, respectively. The white dashed contours mark our 20 K freezeout boundary, while the solid black contours and dashed colored curves show the corresponding emission regions for each analysis. Despite differences in the detailed thermal prescriptions, all models show some regions of temperatures of ∼20–30 K within the CO-emitting layer. The emission is dominated by regions where CO remains in the gas phase, above the freezeout threshold of ∼20 K, typically within $R \sim 200$–300 au. As a result, the local thermal conditions in the emitting layer set the observed CO emission, making it relatively insensitive to the details of the global temperature parameterization.

3.3. CS Fitting

We verify the robustness of the CO-derived disk structure by using it as a base model for the CS $J = 7$–6 emission. The best-fit model (parameters listed in Table 1) reproduces both the channel maps (Figure 5) and the integrated line profile (Figure 2, right), with residuals at the noise level. The integrated line profile for CS is significantly noisier than that of CO, due to its lower abundance and weaker emission, which reduces the signal-to-noise ratio. Similar to our CO comparison, we also plot the spectrum of the best-fitting model with no turbulent contribution (Figure 2, right panel) and once again see that a significant level of nonthermal broadening in the model is required to reproduce the peak emission in the data. We also observe a consistent overprediction of emission near the disk center in all channels (Figure 5), producing a central residual. This likely results from the continuum emission not being modeled accurately—an effect that is negligible for CO but becomes more significant for the weaker CS emission—rather than a fundamental issue with the underlying CO-based disk model. Therefore, we only trust the model at radii larger than the extent of the continuum emission ($R \gtrsim 119$ au).

The inferred CS abundance of $\log_{10}(X_{\rm CS}) \approx -9.4$ corresponds to a CS/CO abundance ratio of order 10^{-5}. The freezeout fraction for CS is $f_{\rm remain} \sim 0.997$, indicating that essentially all CS remains in the gas phase, with freezeout playing a negligible role. In contrast, CO is almost entirely frozen onto grains at temperatures below 20 K ($f_{\rm remain} \sim 0.002$). The CS emission can therefore be reproduced without invoking significant depletion onto grains, and without altering the underlying disk structure derived from CO. This again confirms that the CO-based model provides a reliable framework for interpreting multiple molecular tracers, with chemical differences arising primarily from abundance variations rather than structural uncertainties.

We can also compare our resulting CS model with that of S. Guilloteau et al. (2012), who fit the CS $J = 3$–2 transition using a similar density parameterization but a radially decreasing CS abundance ($4.2 \times 10^{-10} \times (r/300\,{\rm au})^{-0.39}$) and a column density threshold that removes CS from the midplane. Figure 6 shows the comparison of the resulting column densities. Because S. Guilloteau et al. (2012) adopted a decreasing abundance profile, our constant abundance of $X_{\rm CS} = 10^{-9.4}$ yields number densities that are on average similar across the disk, though slightly lower in the inner regions and somewhat higher in the outer disk. To reproduce the observed $J = 7$–6 emission, our model allows CS to remain in the gas phase throughout the disk, effectively turning off freezeout. This behavior is consistent with the findings of S. Guilloteau et al. (2012), who showed that CS can exist at temperatures well below its evaporation temperature (∼30 K). In their study, the vertical extent of the molecular-rich layer was primarily regulated by UV penetration, photodesorption, and photodissociation rather than temperature, with thermal desorption becoming significant only above ∼30 K.

Overall, these results show that the CS $J = 7$–6 emission can be reproduced within the CO-derived disk framework, with differences from the S. Guilloteau et al. (2012) $J = 3$–2 model primarily driven by our lower, constant abundance and the absence of a tunable column density threshold when reproducing photodesorption effects. The persistence of CS down to the midplane indicates that it is not in thermochemical equilibrium, emphasizing the role of chemical processes and UV-driven effects in shaping its vertical distribution, which we will discuss more in Section 4.3.

4. Discussion

4.1. Turbulence in the DM Tau Disk

Our modeling of the ^{12}CO $J = 3$–2 emission in DM Tau constrains the nonthermal contribution to the line width to $f_{\rm turb} = 0.403^{+0.008}_{-0.012} c_s$, corresponding to an average nonthermal

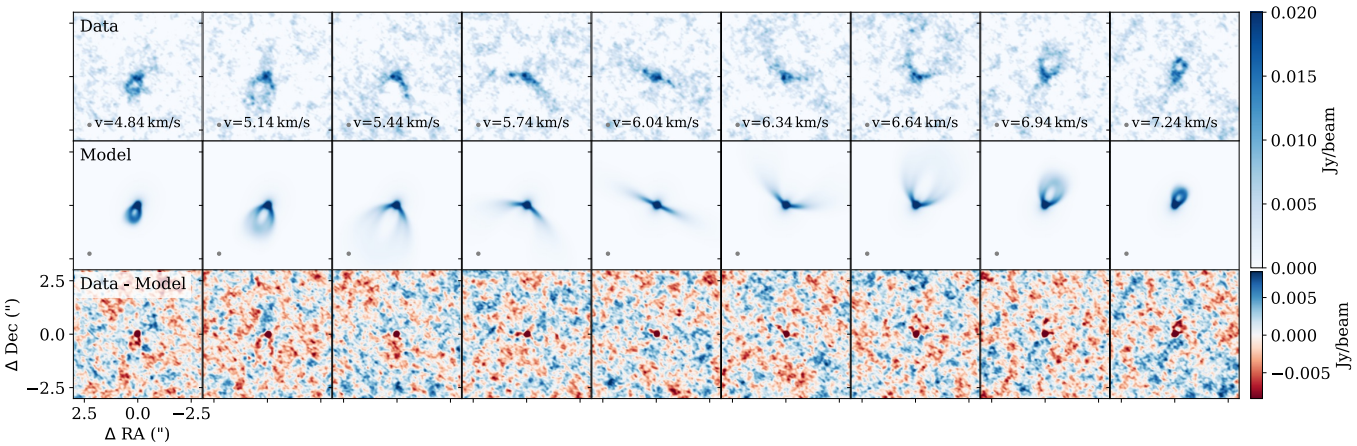

Figure 5. Channel maps of DM Tau in CS $J = 7$–6 emission at 0.″15 resolution. The top row shows the observed data, the middle row the equivalent channels for our best-fit model, and the bottom row the residuals from subtracting this model from the data. The residual color bar represents $\pm 3\sigma$ flux of the data.

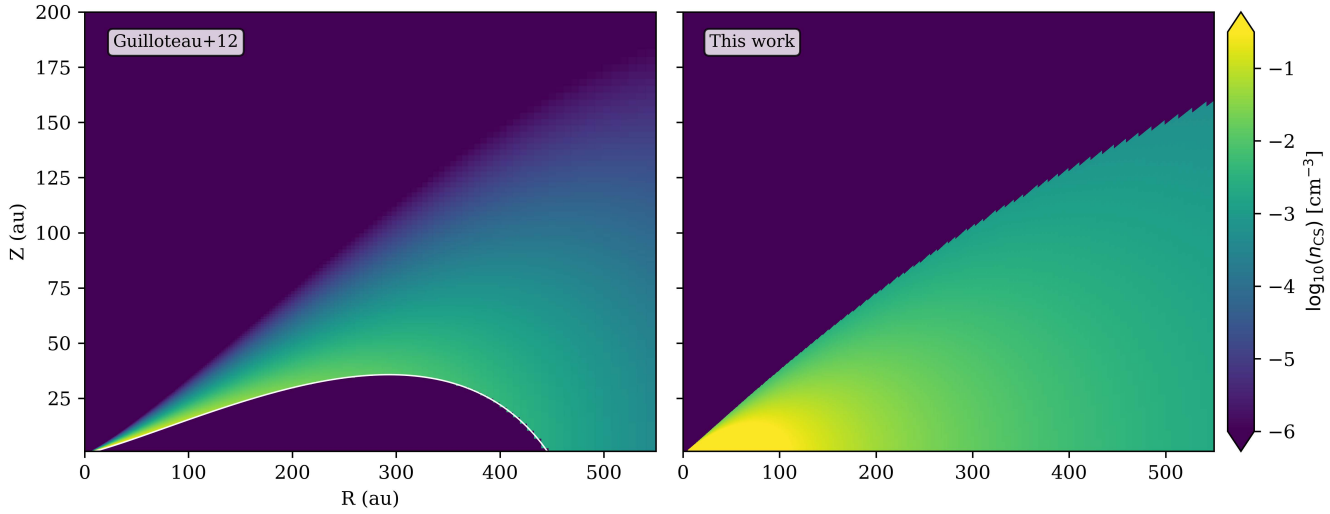

Figure 6. CS number density in DM Tau. Left: CS $J = 3$–2 model from S. Guilloteau et al. (2012), which uses a radially decreasing abundance and a hydrogen column density depletion threshold of $10^{21.7}$ cm^{-2} (white curve). Right: our CS $J = 7$–6 model, adopting a constant abundance $\log10(X_{CS}) = -9.4$ and a freezeout threshold of 30 K.

broadening of $\sim$180 m s^{-1} in the CO-emitting layers. This level of turbulence is significantly higher than previous estimates from the CO $J = 2$–1 transition (K. Flaherty et al. 2020, $0.25c_s$–$0.33c_s$) and inconsistent with a completely laminar disk.

In our model, the nonthermal broadening is parameterized as a fixed fraction of the local sound speed, implying a spatially constant Mach number throughout the emitting region. This approach follows other recent analyses (e.g., K. Flaherty et al. 2020) and provides a convenient way to compare systems, though it likely oversimplifies the true structure of turbulence in disks. Studies that adopt radially varying or nonparametric prescriptions (S. Guilloteau et al. 2012; R. Teague et al. 2016) and numerical simulations (J. B. Simon et al. 2015; M. Barraza-Alfaro et al. 2025) suggest that turbulence generally increases with height above the midplane as instabilities such as the VSI or MRI become more effective. Consequently, our single-parameter description should be viewed as an average measure of the turbulent amplitude within the CO-emitting layers rather than a detailed vertical profile.

The elevated turbulence inferred here may also reflect additional physical and observational effects. Higher-J CO transitions probe warmer, more elevated layers of the disk, which are naturally more dynamic and therefore more susceptible to the kinds of motions driven by the instabilities discussed above. As mentioned in Section 3.2, we do not see a notable difference between the $J = 3$–2 and 2–1 emission surfaces for our models, but compared to the K. Flaherty et al. (2020) model (left panel of Figure 3), our surface in the outer disk is higher, which could be leading to our higher inferred value of f_{turb}. If the disk were fully turbulent, we would expect to observe large-scale deviations from Keplerian rotation at the exoALMA spectral resolution as demonstrated by M. Barraza-Alfaro et al. (2025), but our data do not show such global motions. Instead, localized small-scale motions, potentially induced by embedded planets or local instabilities, may contribute to the line broadening: C. Pinte et al. (2025) identified a potential velocity kink and filamentary structures between the upper and lower disk surfaces in DM Tau that result in subtle deviations from pure Keplerian rotation, the same as those we can identify in our residuals (see Section 4.2.

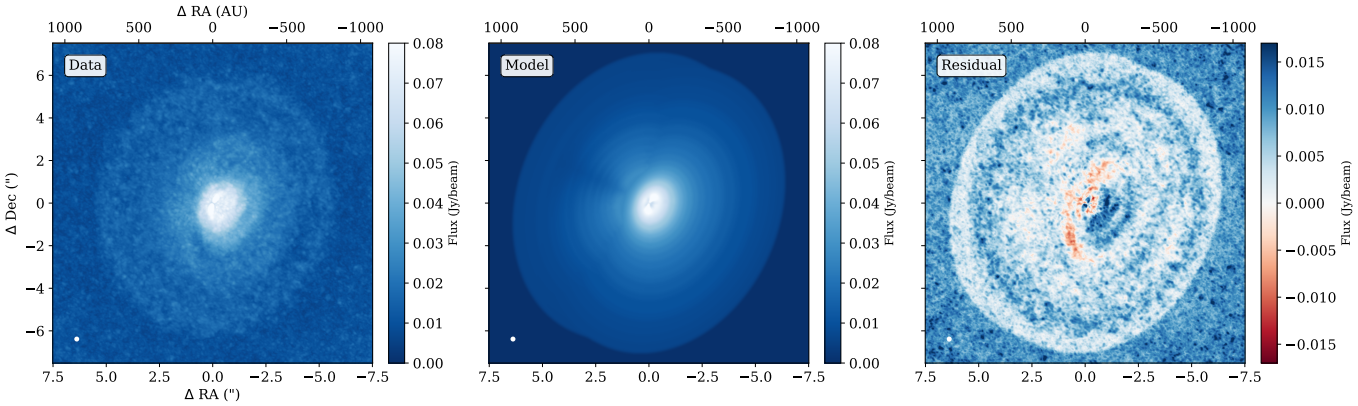

Figure 7. ^{12}CO peak intensity maps. Left: observed data. Middle: best-fit model. Right: residual map (data minus model), highlighting regions where the model over- or underpredicts the emission.

While our high-resolution exoALMA data of DM Tau do not show large-scale non-Keplerian arcs such as those seen around CQ Tau, HD 135344B, J1604, and MWC 758, these localized kinematic features in DM Tau could account for part of the measured nonthermal line width. Taken together, the inferred nonthermal broadening and the absence of global kinematic deviations imply that the observed line widths could reflect localized or small-scale motions, though distinguishing these from genuinely turbulent processes remains challenging.

An important consideration when comparing our gas temperature and turbulence measurements to other studies is the potential effect of amplitude calibration uncertainties. Previous analyses, which derived gas temperatures directly from the observed CO line intensities, such as K. Flaherty et al. (2020), are susceptible to systematic errors when the flux scale is translated directly into temperature uncertainties. This in turn affects the inferred thermal and nonthermal broadening. Our radiative transfer approach is fundamentally different, and while we do not fit explicitly for temperature, flux calibration errors could in principle affect our inferred disk properties.

We performed parameter studies and found that the parameters that dominate the observed line emission in our models are the stellar radius (which sets the luminosity and therefore the temperature structure), the external radiation field (which provides additional heating in the upper disk layers), and the CO abundance (which converts the temperature and density structure into observable emission). We fit all of these parameters simultaneously, and our posterior distributions (Figure 9 in the Appendix) show that they are well constrained without significant degeneracies with each other or with the turbulent broadening, indicating that systematic flux calibration errors are not being absorbed into biases in individual parameters. The variance inflation parameter $\ln q$ further mitigates the impact of systematic flux scale mismatches.

Crucially, our turbulence measurement is constrained primarily by the local line widths rather than the absolute flux level. Since flux calibration errors do not translate directly to temperature uncertainties in our model unlike parametric fits to the data, our turbulence measurement is therefore relatively insensitive to systematic uncertainties in the flux calibration. We therefore expect our turbulence constraints to be robust against amplitude calibration uncertainties at the ∼10%–15% level typical of ALMA observations.

4.2. Substructure in the DM Tau Disk

As mentioned in Section 2.2, we have assumed a smooth disk for DM Tau, as including substructure in the model would drastically widen the parameter space. However, the disk around DM Tau was referred to as a "proto-asteroid belt" by T. Kudo et al. (2018), with ALMA observations of the dust continuum emission revealing that the disk is composed of multiple dust rings and an inner disk (J. Hashimoto et al. 2021; P. Curone et al. 2025). These substructures could reflect the kinematics of the gas in the outer disk, although our modeling does not attempt to capture such effects.

As a result of our smooth model assumption, residual moment maps of the ^{12}CO emission reveal subtle deviations that may provide clues as to the localized dynamical processes in DM Tau. Figures 7 and 8 show examples of these residuals in the peak intensity and velocity maps, respectively, where the model over- or underpredicts the emission or the local line-of-sight velocity in the inner disk. While the origin of the substructures is unclear in these residual maps, the spiral-like morphology may be caused by embedded planets. An outer feature at ∼600 au (4.″2, the dark-blue ring) appears in both moments; its morphology is more consistent with the separation between the front and back CO-emitting surfaces, rather than a true overdensity. Across the disk, the amplitude of these CO residuals reaches 10%–20% of the peak intensity, which demonstrates that even minor deviations from a smooth structure are detectable.

The strength of our approach is in the use of full radiative transfer modeling, which constrains the disk's vertical and thermal structure. While other studies of the exoALMA disks (e.g., M. Barraza-Alfaro et al. 2025; M. Galloway-Sprietsma et al. 2025; A. F. Izquierdo et al. 2025) adopt smooth parametric models as their baseline, our radiative transfer framework provides a physically consistent treatment of temperature, density, and emission. This provides us with a more realistic baseline for identifying residuals from our smooth models and allows subtle dynamical or chemical substructures associated with ongoing planet formation to be identified with greater confidence.

4.3. What Is Causing the CS Emission?

We find that significant CS emission arises from regions of the disk below 30 K, where CS would normally be expected to freeze onto dust grains. In our model, photodesorption is

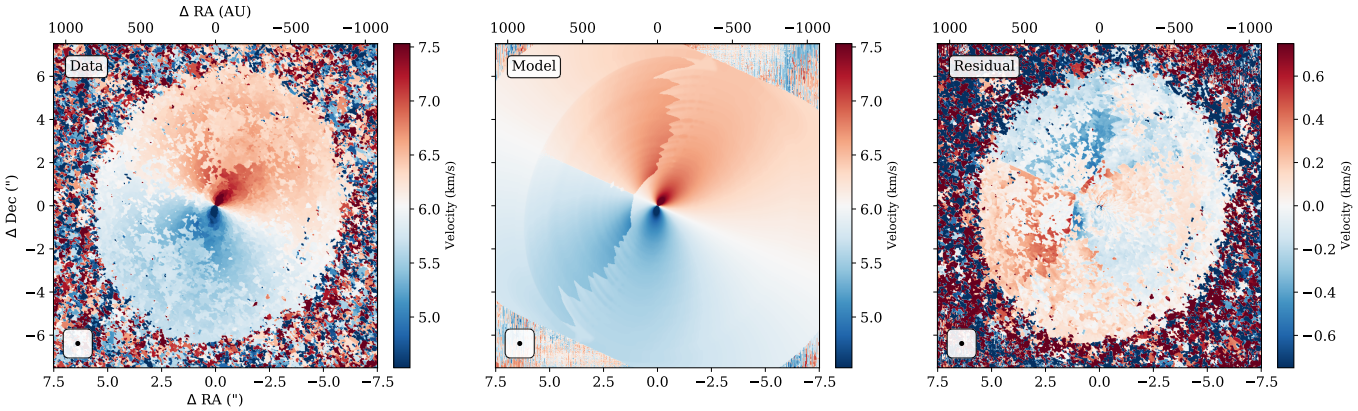

Figure 8. ^{12}CO peak velocity maps. Left: observed data. Middle: best-fit model. Right: residual map (data minus model), showing differences in the velocity of peak emission across the disk.

included but is not strong enough to reproduce the observed $J = 7$–6 emission on its own. Instead, the emission requires that CS remain largely in the gas phase throughout the disk, implying that freezeout is strongly suppressed or that additional nonequilibrium processes act to replenish gas-phase CS in cold regions.

Physically, the $f_{\rm remain}$ parameter may represent the cumulative effect of processes that prevent complete CS depletion in the disk midplane. These could include cosmic-ray or chemical desorption and vertical mixing that transports CS-rich gas from warmer layers. Other mechanisms could also contribute to the formation of CS at low temperatures. For example, shocks caused by planet wakes can destroy CO, liberating atomic carbon, which then reacts with available sulfur to form CS (C. J. Law et al. 2025). A similar process occurs in AGB winds, where CS forms after C is liberated from CO through shocks (I. Cherchneff 2006; T. Danilovich et al. 2019), especially when there is little free C available otherwise.

Comparing our distribution to theoretical chemical models, C. Walsh et al. (2010) found that including photodesorption increases CS abundances to values comparable to those in our model (i.e., $\log 10(X_{\rm CS}) \sim -9$). However, in their model the abundance varies with radius and height, tapering off toward the midplane, while our model assumes a constant abundance and negligible freezeout. This difference may indicate that our simplified prescription effectively compensates for missing nonthermal desorption or mixing processes that maintain CS in the gas phase. A more realistic treatment would likely allow the degree of depletion to vary with both radius and height, since the stellar parameters adopted by C. Walsh et al. (2010) are similar to those used here for DM Tau.

To observationally constrain the dominant mechanisms responsible for sustaining CS, it will be important to study CS emission across a larger sample of disks spanning a range of stellar and disk conditions, including systems with evidence for planetary companions, to determine how the CS distribution varies with disk structure, irradiation environment, and planet–disk interactions.

5. Conclusions

Leveraging the high-resolution ^{12}CO $J = 3$–2 and CS $J = 7$–6 data of the DM Tau disk from the exoALMA survey, we perform full radiative transfer modeling with MCFOST to constrain the disk structure and nonthermal line broadening. We find the following:

1. Our best-fit CO model reproduces both the channel maps and the integrated line profile, yielding a measured nonthermal broadening of $f_{\rm turb} = 0.4c_s$, slightly higher than previously reported.
2. We find that the CS number density in the midplane is very similar to previous models, but due to our model parameterization (using a constant CS abundance and allowing freezeout to be suppressed), it produces emission that extends more uniformly and deeper into the disk. Future work could incorporate a more physically motivated treatment of freezeout and desorption to better capture the underlying chemistry.
3. Residual maps of ^{12}CO (Figure 7) reveal subtle deviations from our smooth disk model, indicating the presence of weak substructures that may trace dynamical perturbations or variations in local chemistry within the DM Tau disk.

By combining high-resolution data from surveys like exoALMA with detailed radiative transfer modeling, it is now possible to better characterize disk turbulence, vertical structure, molecular distributions, and low-level substructures across multiple sources. Applying this approach to other disks would help to reveal trends in disk physics and chemistry and place individual systems such as DM Tau in the broader context of protoplanetary disk evolution and planet formation.

Acknowledgments

C. Har. and T.H. are funded by Research Training Program Scholarships from the Australian Government. C. Har., D.J.P., C.P., T.H., and I.H. acknowledge funding from the Australian Research Council via DP220103767 and DP240103290. C. Har. acknowledges support from the Astronomical Society of Australia. T.D. is supported in part by the Australian Research Council through a Discovery Early Career Researcher Award (DE230100183). G.R. acknowledges funding from the Fondazione Cariplo, grant No. 2022-1217, and the European Research Council (ERC) under the European Union's Horizon Europe Research & Innovation Programme under grant agreement No. 101039651 (DiscEvol). J.B. acknowledges support from NASA XRP grant No. 80NSSC23K1312. M.B., D.F., J.S., and I.H. have received funding from the European Research Council (ERC) under the European Union's Horizon 2020 research and innovation

program (PROTOPLANETS, grant agreement No. 101002188). N.C. has received funding from the European Research Council (ERC) under the European Union Horizon Europe research and innovation program (grant agreement No. 101042275, project Stellar-MADE). P.C. acknowledges support by the ANID BASAL project FB210003. S.F. is funded by the European Union (ERC, UNVEIL, 101076613) and acknowledges financial contribution from PRIN-MUR 2022YP5ACE. M.Fl. has received funding from the European Research Council (ERC) under the European Unions Horizon 2020 research and innovation program (grant agreement No. 757957). M.Fu. is supported by a grant-in-aid from the Japan Society for the Promotion of Science (KAKENHI: No. JP22H01274). C. Hal. gratefully acknowledges support from the US National Science Foundation grants 2511673 and 2407679, NRAO SOSPADA-036, National Geographic Society, and the Georgia Museum of Natural History. J.D.I. acknowledges support from an STFC Ernest Rutherford Fellowship (ST/W004119/1) and a University Academic Fellowship from the University of Leeds. Support for A.F.I. was provided by NASA through NASA Hubble Fellowship grant No. HST-HF2-51532.001-A awarded by the Space Telescope Science Institute, which is operated by the Association of Universities for Research in Astronomy, Inc., for NASA, under contract NAS5-26555. G.Le. and G.W.-F. have received funding from the European Research Council (ERC) under the European Union Horizon 2020 research and innovation program (grant agreement No. 815559 (MHDiscs)). G.W.-F. was granted access to the HPC resources of IDRIS under the allocation A0120402231 made by GENCI. C.L. and G.Lo. have received funding from the European Union's Horizon 2020 research and innovation program under the Marie Sklodowska-Curie grant agreement No. 823823 (DUSTBUSTERS). C.L. acknowledges support from the UK Science and Technology research Council (STFC) via the consolidated grant ST/W000997/1. F.Me. acknowledges funding from the European Research Council (ERC) under the European Union's Horizon Europe research and innovation program (grant agreement No. 101053020, project Dust2Planets). H.-W.Y. acknowledges support from the National Science and Technology Council (NSTC) in Taiwan through grant NSTC 113-2112-M-001-035- and from the Academia Sinica Career Development Award (AS-CDA-111-M03). T.C.Y. is supported by Grant-in-Aid for JSPS Fellows JP23KJ1008. A.J.W. has been supported by the European Union's Horizon 2020 research and innovation program (Marie Sklodowska-Curie grant agreement No. 101104656) and by the Royal Society through a University Research Fellowship, grant No. URF\R1\241791. Support for B.Z. was provided by the Brinson Foundation. Views and opinions expressed by ERC-funded scientists are, however, those of the author(s) only and do not necessarily reflect those of the European Union or the European Research Council. Neither the European Union nor the granting authority can be held responsible for them. This Letter makes use of the following ALMA data: ADS/JAO.ALMA#2021.1.01123.L. ALMA is a partnership of ESO (representing its member states), NSF (USA) and NINS (Japan), together with NRC (Canada), MOST and ASIAA (Taiwan), and KASI (Republic of Korea), in cooperation with the Republic of Chile. The Joint ALMA Observatory is operated by ESO, AUI/NRAO and NAOJ. This work was performed on the OzSTAR national facility at Swinburne University of Technology. The OzSTAR program receives funding in part from the Astronomy National Collaborative Research Infrastructure Strategy (NCRIS) allocation provided by the Australian Government and from the Victorian Higher Education State Investment Fund (VHESIF) provided by the Victorian Government.

Software: bettermoments (R. Teague & D. Foreman-Mackey 2018), Matplotlib (J. D. Hunter 2007), NumPy (C. R. Harris et al. 2020), SciPy (P. Virtanen et al. 2020) and Astropy (Astropy Collaboration et al. 2013, 2018, 2022).

Appendix
Posterior Results

Here we present some additional plots showing details of the MCMC fits. Figure 9 shows our 1D and 2D posteriors, and Figure 10 shows the walker progression plots for our fit to the CO emission. See Section 3.1 for discussion of these results.

Figure 11 shows our 1D and 2D posteriors, and Figure 12 shows the walker progression plots for our fit to the CS emission. See Section 3.3 for discussion of these results.

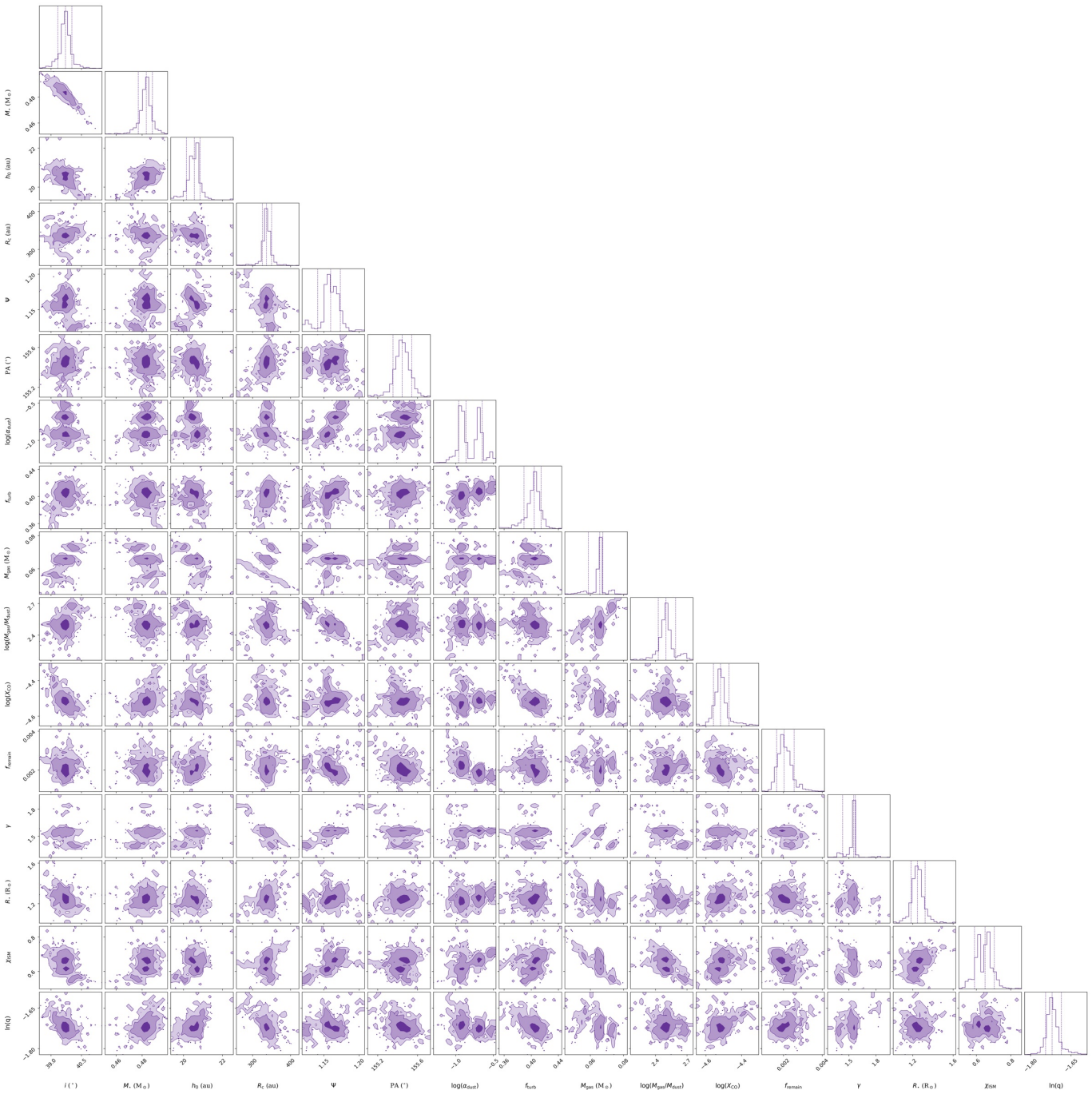

Figure 9. Marginalized 1D and 2D posterior distributions of the CO emission fit. Vertical lines in the 1D distributions mark the 10th, 50th, and 90th percentiles.

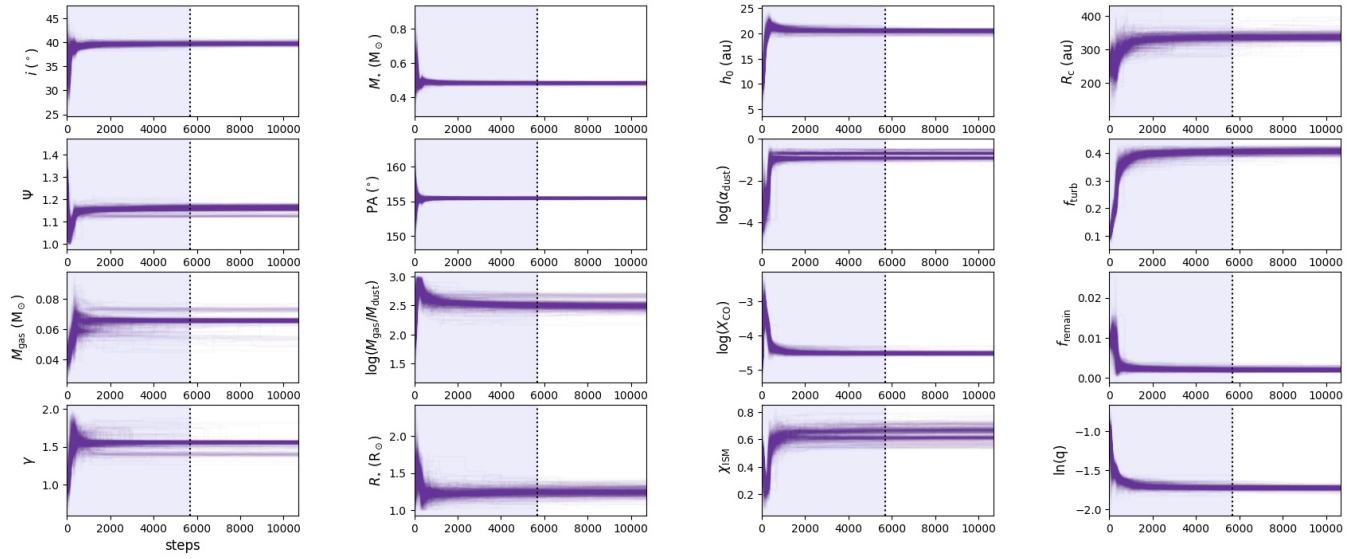

Figure 10. Walker progression for the fit to the CO emission. The vertical dotted line indicates the transition between the burn-in and sampling phases; the burn-in region (shaded in purple) is discarded prior to calculating median parameter values.

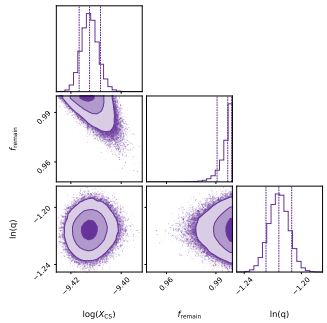

Figure 11. Marginalized 1D and 2D posterior distributions of the CS emission fit. Vertical lines in the 1D distributions mark the 10th, 50th, and 90th percentiles.

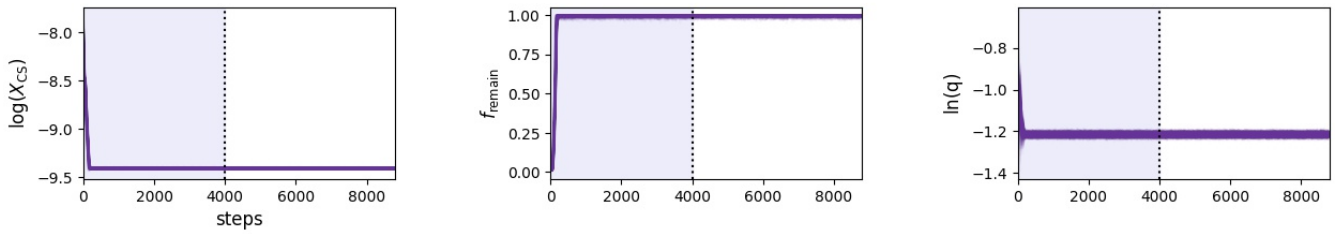

Figure 12. Same as Figure 10, but for the fit to the CS emission.

ORCID iDs

Caitlyn Hardiman https://orcid.org/0009-0003-7403-9207
Christophe Pinte https://orcid.org/0000-0001-5907-5179
Daniel J. Price https://orcid.org/0000-0002-4716-4235
Thomas Hilder https://orcid.org/0000-0001-7641-5235
Iain Hammond https://orcid.org/0000-0003-1502-4315
Taïssa Danilovich https://orcid.org/0000-0002-1283-6038
Sean M. Andrews https://orcid.org/0000-0003-2253-2270
Richard Teague https://orcid.org/0000-0003-1534-5186
Giovanni Rosotti https://orcid.org/0000-0003-4853-5736
Mario Flock https://orcid.org/0000-0002-9298-3029
Gianni Cataldi https://orcid.org/0000-0002-2700-9676
Jaehan Bae https://orcid.org/0000-0001-7258-770X
Marcelo Barraza-Alfaro https://orcid.org/0000-0001-6378-7873
Myriam Benisty https://orcid.org/0000-0002-7695-7605
Nicolás Cuello https://orcid.org/0000-0003-3713-8073
Pietro Curone https://orcid.org/0000-0003-2045-2154
Ian Czekala https://orcid.org/0000-0002-1483-8811
Stefano Facchini https://orcid.org/0000-0003-4689-2684
Daniele Fasano https://orcid.org/0000-0003-4679-4072
Misato Fukagawa https://orcid.org/0000-0003-1117-9213
Maria Galloway-Sprietsma https://orcid.org/0000-0002-5503-5476
Himanshi Garg https://orcid.org/0000-0002-5910-4598

Cassandra Hall https://orcid.org/0000-0002-8138-0425
Jane Huang https://orcid.org/0000-0001-6947-6072
John D. Ilee https://orcid.org/0000-0003-1008-1142
Andres F. Izquierdo https://orcid.org/0000-0001-8446-3026
Kazuhiro Kanagawa https://orcid.org/0000-0001-7235-2417
Geoffroy Lesur https://orcid.org/0000-0002-8896-9435
Giuseppe Lodato https://orcid.org/0000-0002-2357-7692
Cristiano Longarini https://orcid.org/0000-0003-4663-0318
Ryan Loomis https://orcid.org/0000-0002-8932-1219
Francois Menard https://orcid.org/0000-0002-1637-7393
Ryuta Orihara https://orcid.org/0000-0003-4039-8933
Jochen Stadler https://orcid.org/0000-0002-0491-143X
Hsi-Wei Yen https://orcid.org/0000-0003-1412-893X
Gaylor Wafflard- Fernandez https://orcid.org/0000-0002-3468-9577
David J. Wilner https://orcid.org/0000-0003-1526-7587
Andrew J. Winter https://orcid.org/0000-0002-7501-9801
Lisa Wölfer https://orcid.org/0000-0002-7212-2416
Tomohiro C. Yoshida https://orcid.org/0000-0001-8002-8473
Brianna Zawadzki https://orcid.org/0000-0001-9319-1296

References

Akaike, H. 1974, ITAC, 19, 716
Andrews, S. M., Wilner, D. J., Espaillat, C., et al. 2011, ApJ, 732, 42
Astropy Collaboration, Price-Whelan, A. M., Lim, P. L., et al. 2022, ApJ, 935, 167
Astropy Collaboration, Price-Whelan, A. M., Sipőcz, B. M., et al. 2018, AJ, 156, 123
Astropy Collaboration, Robitaille, T. P., Tollerud, E. J., et al. 2013, A&A, 558, A33
Balbus, S. A., & Hawley, J. F. 1991, ApJ, 376, 214
Balbus, S. A., & Hawley, J. F. 1998, RvMP, 70, 1
Barraza-Alfaro, M., Flock, M., Béthune, W., et al. 2025, ApJL, 984, L21
Cherchneff, I. 2006, A&A, 456, 1001
Curone, P., Facchini, S., Andrews, S. M., et al. 2025, ApJL, 984, L9
Danilovich, T., Richards, A. M. S., Karakas, A. I., et al. 2019, MNRAS, 484, 494
Dorschner, J., Begemann, B., Henning, T., Jaeger, C., & Mutschke, H. 1995, A&A, 300, 503
Draine, B. T. 1978, ApJS, 36, 595
Dubrulle, B., Morfill, G., & Sterzik, M. 1995, Icar, 114, 237
Duchêne, G., Ménard, F., Stapelfeldt, K. R., et al. 2024, AJ, 167, 77
Flaherty, K., Hughes, A. M., Simon, J. B., et al. 2020, ApJ, 895, 109
Flaherty, K., Hughes, A. M., Simon, J. B., et al. 2024, MNRAS, 532, 363
Flaherty, K. M., Hughes, A. M., Rose, S. C., et al. 2017, ApJ, 843, 150
Flaherty, K. M., Hughes, A. M., Rosenfeld, K. A., et al. 2015, ApJ, 813, 99
Flaherty, K. M., Hughes, A. M., Teague, R., et al. 2018, ApJ, 856, 117
Flock, M., Nelson, R. P., Turner, N. J., et al. 2017, ApJ, 850, 131
Foreman-Mackey, D., Hogg, D. W., Lang, D., & Goodman, J. 2013, PASP, 125, 306
Francis, L., Marel, N. v. d., Johnstone, D., et al. 2022, AJ, 164, 105
Fromang, S., & Nelson, R. P. 2009, A&A, 496, 597
Gaia Collaboration, Vallenari, A., Brown, A. G. A., et al. 2023, A&A, 674, A1
Galloway-Sprietsma, M., Bae, J., Izquierdo, A. F., et al. 2025, ApJL, 984, L10
Garrod, R. T., & Herbst, E. 2006, A&A, 457, 927
Goodman, J., & Rafikov, R. R. 2001, ApJ, 552, 793
Guilloteau, S., Dutrey, A., Wakelam, V., et al. 2012, A&A, 548, A70
Harris, C. R., Millman, K. J., van der Walt, S. J., et al. 2020, Natur, 585, 357
Hartmann, L., Calvet, N., Gullbring, E., & D'Alessio, P. 1998, ApJ, 495, 385
Hashimoto, J., Muto, T., Dong, R., et al. 2021, ApJ, 911, 5
Hilder, T., Casey, A. R., Price, D. J., et al. 2025, ApJL, 984, L13
Hughes, A. M., Wilner, D. J., Andrews, S. M., Qi, C., & Hogerheijde, M. R. 2011, ApJ, 727, 85
Hunter, J. D. 2007, CSE, 9, 90
Izquierdo, A. F., Stadler, J., Galloway-Sprietsma, M., et al. 2025, ApJL, 984, L8
Izquierdo, A. F., Testi, L., Facchini, S., Rosotti, G. P., & van Dishoeck, E. F. 2021, A&A, 650, A179
Kratter, K., & Lodato, G. 2016, ARA&A, 54, 271
Kudo, T., Hashimoto, J., Muto, T., et al. 2018, ApJL, 868, L5
Law, C. J., Le Gal, R., Yamato, Y., et al. 2025, ApJ, 985, 84
Le Gal, R., Öberg, K. I., Loomis, R. A., Pegues, J., & Bergner, J. B. 2019, ApJ, 876, 72
Longarini, C., Lodato, G., Rosotti, G., et al. 2025, ApJL, 984, L17
Loomis, R. A., Facchini, S., Benisty, M., et al. 2025, ApJL, 984, L7
Lynden-Bell, D., & Pringle, J. E. 1974, MNRAS, 168, 603
Manara, C. F., Ansdell, M., Rosotti, G. P., et al. 2023, ASPC, 534, 539
Manara, C. F., Rosotti, G., Testi, L., et al. 2016, A&A, 591, L3
Manara, C. F., Testi, L., Natta, A., et al. 2014, A&A, 568, A18
Min, M., Hovenier, J. W., & de Koter, A. 2005, A&A, 432, 909
Nelson, R. P., Gressel, O., & Umurhan, O. M. 2013, MNRAS, 435, 2610
Paneque-Carreño, T., Izquierdo, A. F., Teague, R., et al. 2024, A&A, 684, A174
Pfeil, T., & Klahr, H. 2019, ApJ, 871, 150
Pinte, C., Dent, W. R. F., Ménard, F., et al. 2016, ApJ, 816, 25
Pinte, C., Harries, T. J., Min, M., et al. 2009, A&A, 498, 967
Pinte, C., Ilee, J. D., Huang, J., et al. 2025, ApJL, 984, L15
Pinte, C., Ménard, F., Duchêne, G., & Bastien, P. 2006, A&A, 459, 797
Pinte, C., Ménard, F., Duchêne, G., et al. 2018, A&A, 609, A47
Pringle, J. E. 1981, ARA&A, 19, 137
Rosotti, G. P. 2023, NewAR, 96, 101674
Shakura, N. I., & Sunyaev, R. A. 1973, A&A, 24, 337
Simon, J. B., Hughes, A. M., Flaherty, K. M., Bai, X.-N., & Armitage, P. J. 2015, ApJ, 808, 180
Stadler, J., Benisty, M., Winter, A. J., et al. 2025, ApJL, 984, L11
Stoll, M. H. R., & Kley, W. 2014, A&A, 572, A77
Teague, R., Benisty, M., Facchini, S., et al. 2025, ApJL, 984, L6
Teague, R., & Foreman-Mackey, D. 2018, RNAAS, 2, 173
Teague, R., Guilloteau, S., Semenov, D., et al. 2016, A&A, 592, A49
Teague, R., Law, C. J., Huang, J., & Meng, F. 2021, JOSS, 6, 3827
van der Marel, N., Birnstiel, T., Garufi, A., et al. 2021, AJ, 161, 33
van der Plas, G., Casassus, S., Ménard, F., et al. 2014, ApJL, 792, L25
Villenave, M., Ménard, F., Dent, W. R. F., et al. 2020, A&A, 642, A164
Villenave, M., Rosotti, G. P., Lambrechts, M., et al. 2025, A&A, 697, A64
Villenave, M., Stapelfeldt, K. R., Duchêne, G., et al. 2022, ApJ, 930, 11
Villenave, M., Stapelfeldt, K. R., Duchêne, G., et al. 2024, ApJ, 975, 235
Virtanen, P., Gommers, R., Oliphant, T. E., et al. 2020, NatMe, 17, 261
Walsh, C., Millar, T. J., & Nomura, H. 2010, ApJ, 722, 1607
Woitke, P., Min, M., Pinte, C., et al. 2016, A&A, 586, A103
Zubko, V. G., Mennella, V., Colangeli, L., & Bussoletti, E. 1996, MNRAS, 282, 1321